Science Advances

AAAS

Supplementary Materials for

Ultraflexible nanoelectronic probes form reliable, glial scar–free neural integration

Lan Luan, Xiaoling Wei, Zhengtuo Zhao, Jennifer J. Siegel, Ojas Potnis, Catherine A. Tuppen, Shengqing Lin, Shams Kazmi, Robert A. Fowler, Stewart Holloway, Andrew K. Dunn, Raymond A. Chitwood, Chong Xie

The PDF file includes:

- table S1. Animal- and probe-specific recording performance over time.
- Legends for movies S1 to S5
- References (*46, 47*)

Other Supplementary Material for this manuscript includes the following:
(available at advances.sciencemag.org/cgi/content/full/3/2/e1601966/DC1)

- movie S1 (.avi format). A typical implantation procedure of the NET probe.
- movie S2 (.avi format). The NET-vasculature integration 2 months after implantation.
- movie S3 (.avi format). In vivo 2P images of inactive astrocytes and intact capillary network around a folded segment of a NET-50 probe 3 months after implantation.
- movie S4 (.avi format). In vivo 2P images of neurons and two NET-10 probes 1.5 and 2.5 months after implantation.
- movie S5 (.avi format). 3D reconstruction of in vivo 2P images of neurons and two NET-10 probes 1.5 months after implantation (the same images as in movie S4, left).
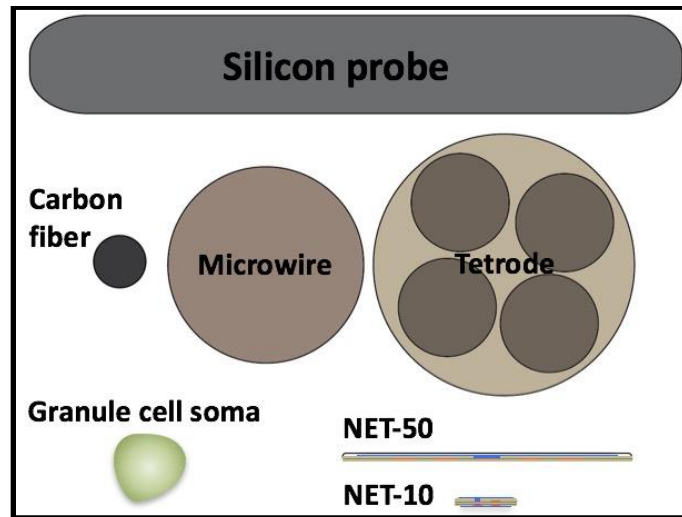
fig. S1. Sketch showing the subcellular cross-section areas of the NET probes in comparison with other representative neural probes, including tetrodes (*1*), microwires (*2*), silicon probes (*3, 4*), and carbon fiber probes (*21*), as well as the soma of a granule cell, which represents the smallest neurons.
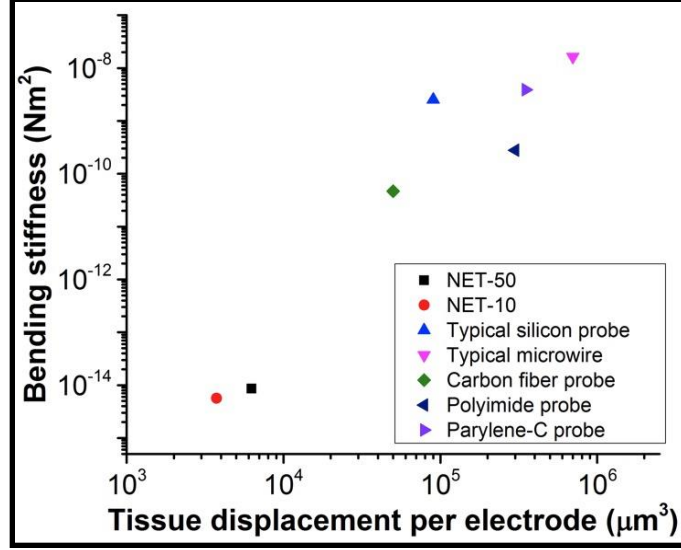
fig. S2. Drastically reduced bending stiffness and tissue displacement per electrode of the NET probes compared with other representative neural probes (silicon (*3*), micro-wire (*2, 46*), carbon fiber (*21*), polyimide (*47*), and parylene-C (*19*)). The bending stiffness K is calculated using geometrical parameters listed in the reference. For shaft-shaped probes, $K_s = E_s wh^3/12$ (eq. S**1**), where E_s is the Young's modulus of the shaft material, h and w are the thickness and the width of the shaft. For cylindrical probes, $K_w = E_w \pi d^4/64$ (eq. S**2**), where E_W is the Young's modulus of the wire/fiber material, d is the diameter of the wire. For the NET probes where the thickness of the insulating layers (SU-8) is comparable to that of the interconnect metal layers, we modify eq. S**1** for better accuracy: $K_{NET} = E_{SU8}\left(\frac{h^3 w}{12} - \frac{h_m^3 w_m}{12}\right) + E_m \frac{h_m^3 w_m}{12}$ (eq. S**3**). E_{SU8} and E_m are the Young's modulus of SU-8 and gold layers respectively; h *and* h_m are the thickness of the SU-8 in total and the gold ($h = 1$ µm, $h_m= 100$ nm); w is the probe width (50 µm for NET-50 and 10 µm and NET-10) and w_m is the total width of gold interconnects (25 µm and 5 µm). TD/E is estimated assuming 1 mm implantation depth for all probes, e.g. TD/E equals to the average cross-section area multiplied by the implanted length and divided by the number of electrodes on the probe.
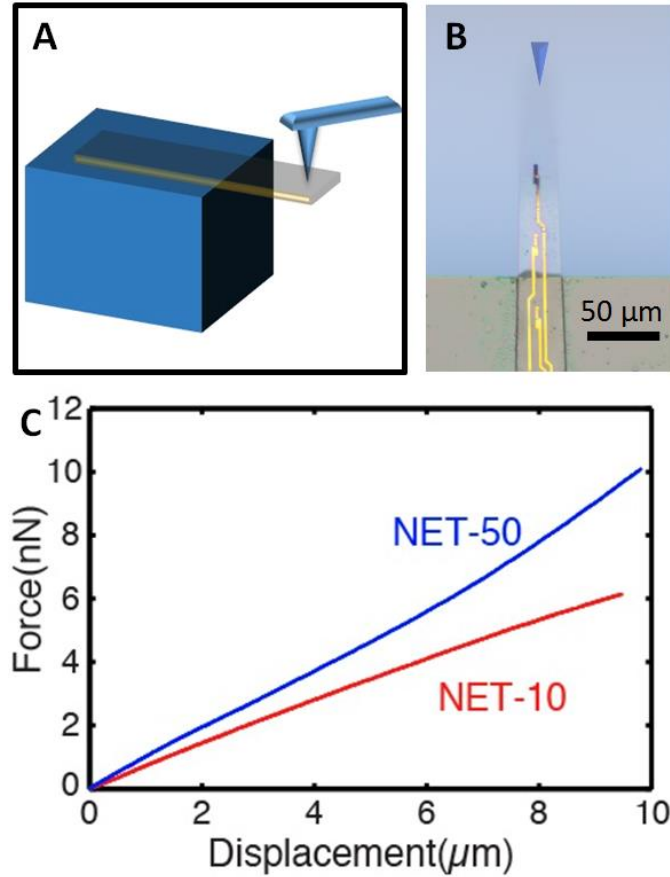
fig. S3. In vitro measurement of the bending force from suspended NET probes. (**A**) Schematic of the measurement using atomic force microscopy (AFM). (**B**) Photograph of a suspended NET-50 probe in air. Blue cone illustrates the position of the AFM tip in the measurement. Scale bar: 50 µm. (**C**) Force-displacement plots for both NET probes measured, giving slopes of 1.0 nN/µm for NET-50 and 0.61 nN/ µm for NET-10. The suspended section length is about 400 µm for both probes. Using the bending stiffness we obtain in fig. S2 (for NET-50 $K = 8.5 \times 10^{-15} N \cdot m^2$ and for NET-10 $K = 5.5 \times 10^{-15} N \cdot m^2$), we calculate the deflection force $F = 8eK/l^3$ to be 10.6 nN and 6.8 nN for NET-50 and NET-10 probes respectively, assuming deflection $e = 10$ µm and probe length $l = 400$ µm, in good agreement with the AFM measurements. The forces are comparable to single cell traction forces (*27*).
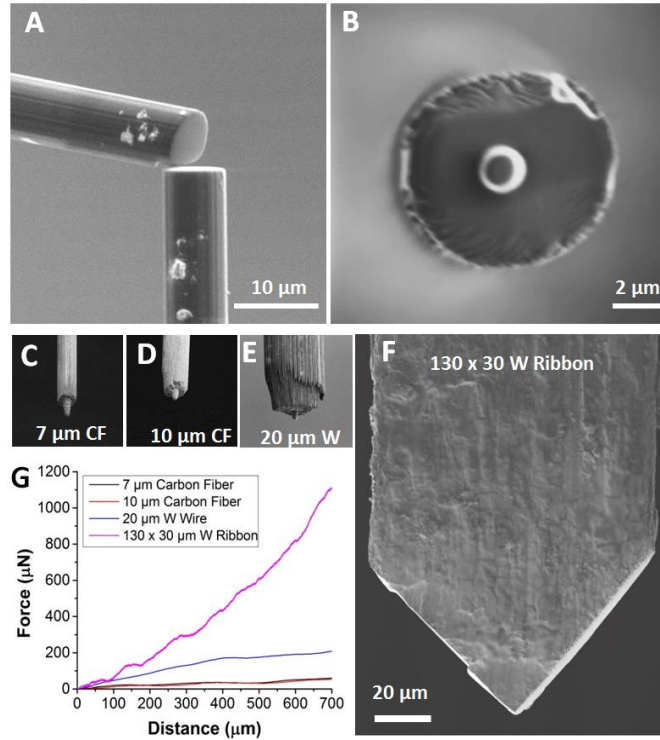
fig. S4. Shuttle device fabrication and in vivo insertion force measurement. (**A**)(**B**) Scanning electron microscopy (SEM) images showing fabrication process of shuttle devices using focused ion beam (FIB). First, a carbon fiber was cut to the desired length ((A) bottom beam). The cut-off segment ((A) top) was attached by electrostatic force, which later fell off when taken out of the vacuum chamber of the FIB. Then a micro-post was milled at the cross-section (B). (**C**) – (**E**) SEM images of three shuttle devices of different dimensions ((C) 7 µm carbon fiber; (D) 10 µm carbon fiber; and (E) 20 µm tungsten micro-wire). (**F**) A 130 µm × 30 µm micro-ribbon to represent the typical dimensions of conventional silicon probes. Images (C) – (F) are resized to the same scale and share the same scale bar in (F). (**G**) *In vivo* measurements of insertion force showing marked reduction (up to ca. 20 fold) from the ultra-small shuttle devices (C) – (E) compared with the conventional probe (F), which suggests greatly reduced acute tissue damage. Insertion force was recorded by a pre-calibrated micro-loading cell mounted at the end of a micro-manipulator holding the shuttle device. Each device was inserted into living mouse cortex at a speed of 10 µm/s for 700 µm. The same procedure was repeated at 3 – 5 different locations for averaging. The force measured from (F) agrees with previously published results using conventional probes (*26*).
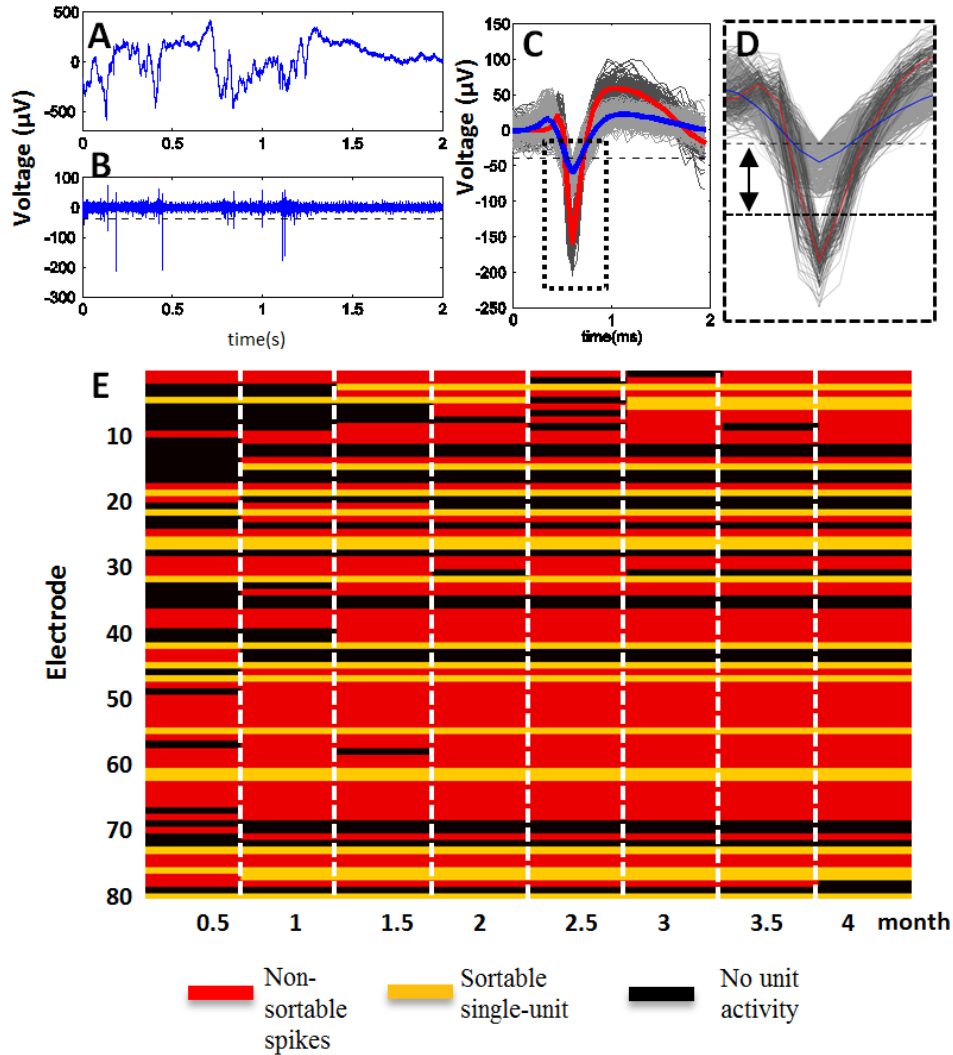
fig. S5. Typical unit recording examples and their detection consistency over 4 months. (**A**)(**B**) Representative raw biopotentials recorded by a NET-50 probe three months post-surgery (A), and with 300 Hz high pass filter applied (B). The dashed line in (B) marks the unit activity detection threshold (-40 µV). (**C**) Superimposed detected unit activities from the same recording session shown in (A) and (B) (9 minutes total). (**D**) Zoom-in view of the boxed area in (C). Unit events cluster into two distinct groups plotted in light gray and dark gray with the mean waveforms for each plotted in blue and red, respectively. The events in dark gray are "sortable" in that their waveforms are clearly separated from the light gray events with no overlap, demonstrating clean separation (marked by dashed lines and the arrow in (D)) of this single unit from background (nearby) multi-unit activity. Sortable single units were found in ~25% of electrodes (Fig. 3(B)). In contrast, the events in light gray, although having sufficient amplitude for spike detection, do not form an isolated cluster above background as their amplitude overlaps with the threshold, and therefore does not represent single-unit activity. Such multi-unit activity was observed in ~75% of the

electrodes (Fig. 3(B)). **(E)** Block chart illustrating non-sortable (multi-unit) spikes and sortable single-unit APs detected by the 80 implanted electrodes as a function of time. Electrode number is marked on the left and measurement time on the bottom. Color code: black, no unit activity detected; red, non-sortable spikes detected; orange, single-unit APs detected in addition to non-sortable spikes. Most changes in recording activities happened within the first month.
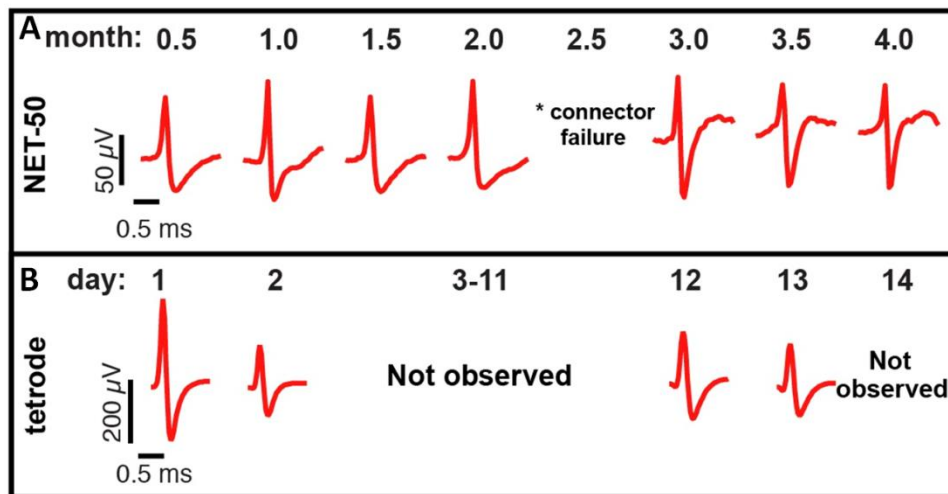

fig. S6. Interneuron recording and tracking compared between a NET-50 electrode and a tetrode. Note the difference in time points between the top and bottom panel (4 months vs. 2 weeks). Single unit activity from interneurons serves as a reliable marker for recording stability because interneurons have a unique waveform (short peak-to-valley width, <350 µs (*34*)) relative to excitatory neurons and typically represents < 10% of the recorded population. **(A)** Interneuron AP waveforms recorded by a NET-50 probe persisted for at least 2 months. **(B)** As a comparison, representative interneuron recording from a chronically implanted tetrode showed sudden absence and significant day-to-day waveform changes over a two-week period.
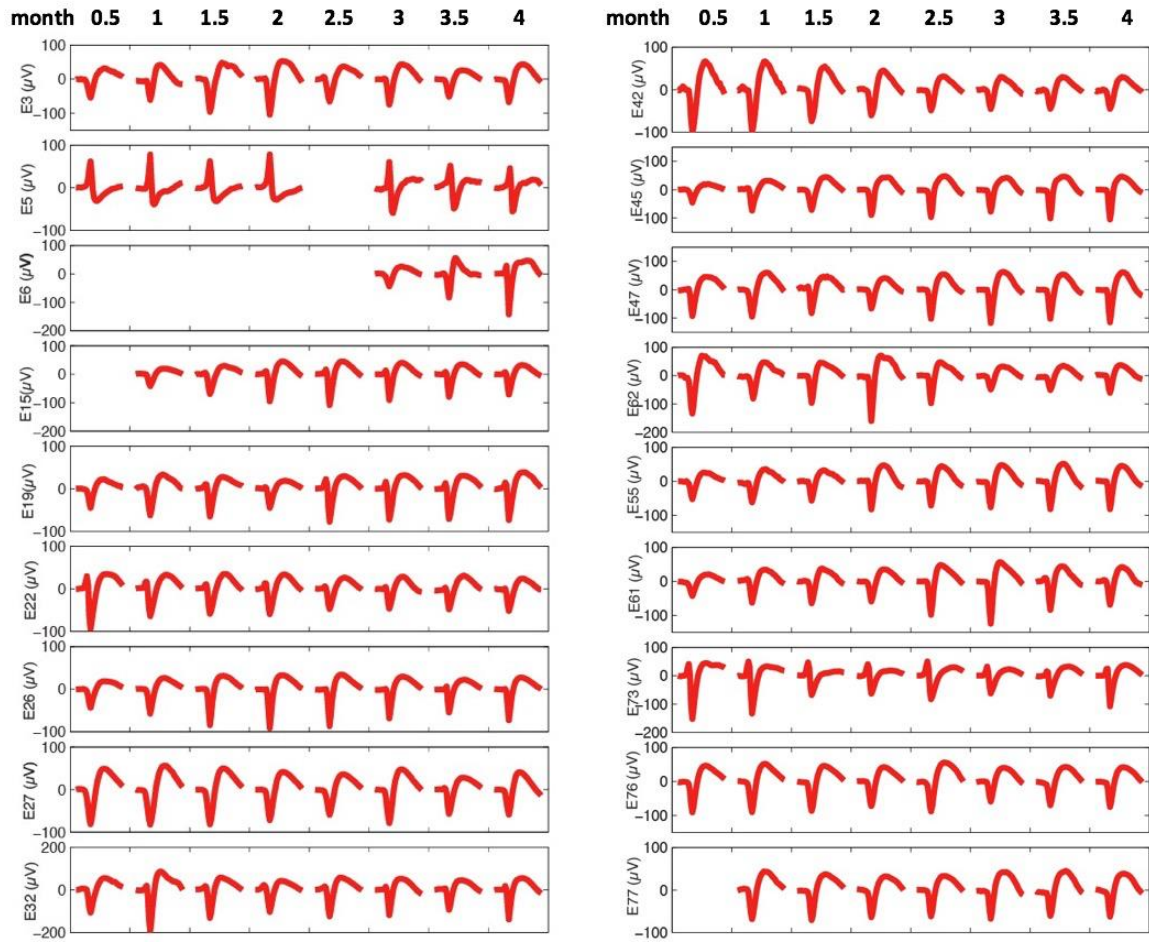
fig. S7. Twice-a-month measurements for 4 months from all electrodes that recorded sortable single-unit APs in addition to the one shown in Fig. 3 (electrode number marked on the left, time post-surgery marked on the top). E5 shows the same data as plotted in fig. S6. All except one (E6) show that same characteristics of the specific waveforms persisted while some more minor but trackable changes occurred. For E6, no unit activities were recorded for 2.5 months after which single-unit APs appeared with substantial changes in waveforms between bi-weekly measurements.
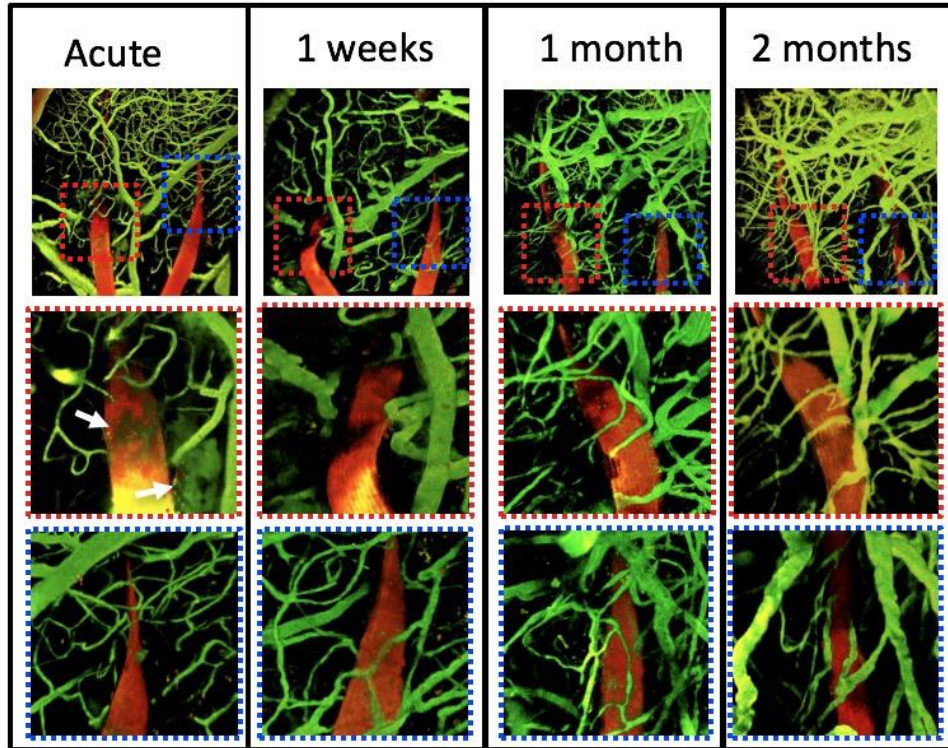
fig. S8. 3D reconstruction of 2P images of the capillary networks (green) surrounding two NET-50 probes (red) at acute, 1 week, 1 month, and 2 months after implantation. Top row: 3D reconstruction of 500 µm × 500 µm image stacks 0 – 400 µm from brain surface and below. Red and blue dashed squares mark the region in the middle and bottom rows. Middle and bottom rows**:** zoom-in views of regions marked in images in the top row. At acute, local leakage in BBB was observed (highlighted by arrows), which was significantly reduced after 1 week and completely disappeared after one month. It is also evident that the NET probe underwent position changes in the first month post implantation when significant vasculature remodeling occurred. The changes were minor after 1 month.
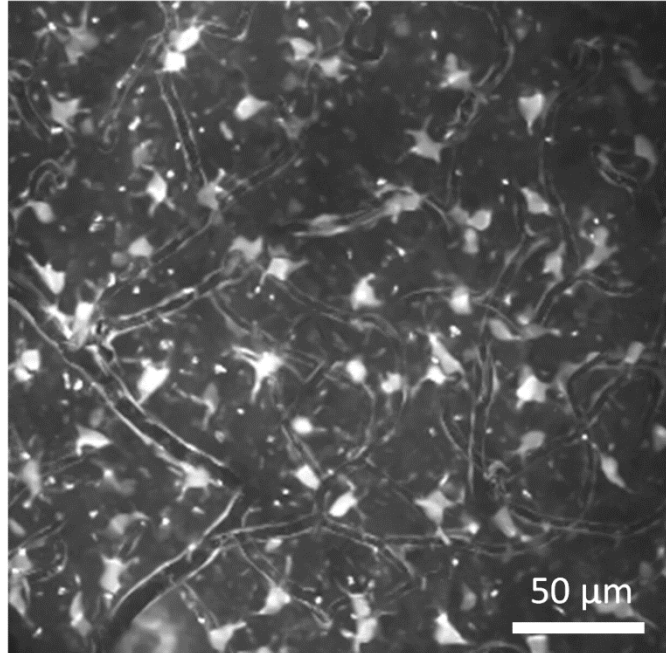
**fig. S9. Z projections of in vivo 2P images of astrocytes from the contralateral hemisphere of the same mouse as in Fig. 4E** showing the astrocytes had similar density and morphology away and around the brain probe. Image depth and position: 100 – 300 µm from brain surface and below.
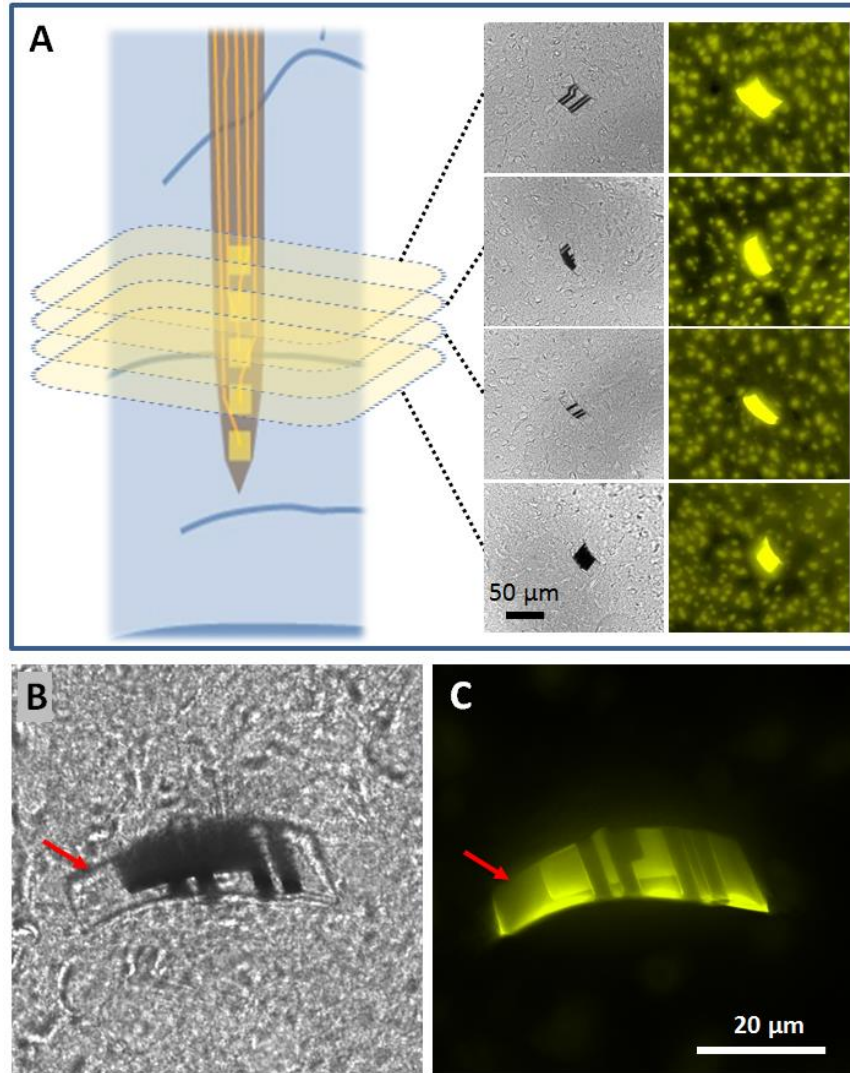
fig. S10. Bright-field and fluorescent images of postmortem tissue slices at the probe-tissue interface 5 months after implantation. (**A**) Images from four consecutive 30-µm-thick slices that were immunochemically labelled. Left panel illustrates the slicing direction relative to brain tissue and the implanted NET probe. Consistent with the *in vivo* imaging shown in Fig. 4, no changes in neuronal density near the probe were observed. Yellow: NeuN, labelling neuron nuclei and Rhodamine 6G, labelling the probe. (**B**)(**C**) Zoom-in view of a typical piece of NET-50 probe embedded in tissue slice in bright field (B) and fluorescence (C). Arrow denotes the probe. Intact device with no cracking or delamination was observed in all slices, showing superior structural and mechanical stability of the NET probes in long-term physiological conditions, which is consistent with the reliable functionality discussed in the manuscript.
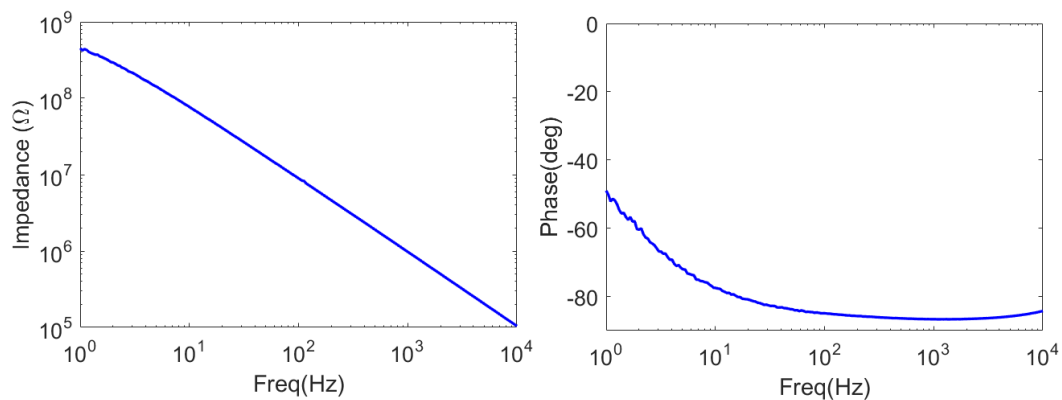
fig. S11. In vitro EIS of a NET electrode that was soaked in saline at 37°C for 35 days. Both the amplitude and the phase dependence of frequency were consistent with moderately capacitive circuit, suggesting that the resistive leakage was limited.
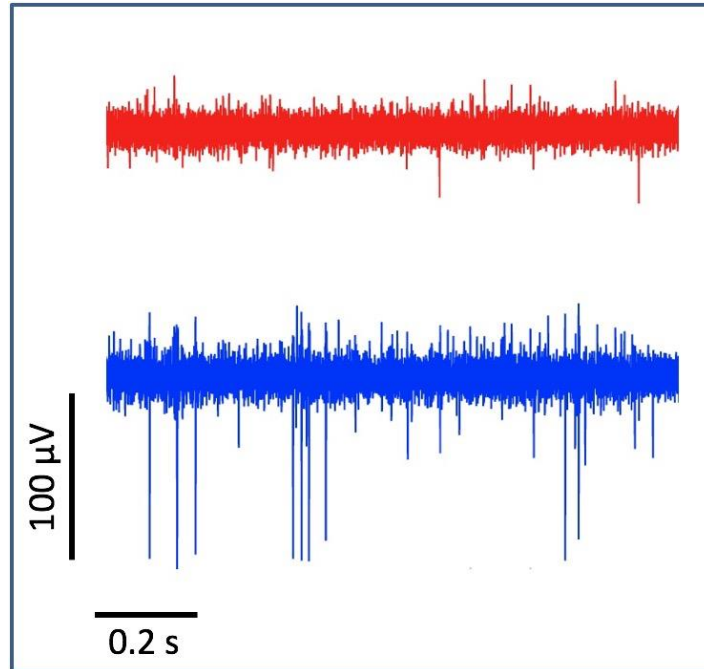
fig. S12. Real-time recording trace (300 Hz high-pass filter applied) from two adjacent channels showing distinct features and little cross-talk. The recording was acquired from a NET probe implanted in the visual cortex of a mouse for 4 months. Distinct recording features in adjacent electrodes were observed here, suggesting that the cross-talk among nearby electrodes was limited, which was representative for all 80 implanted electrodes in this study.

table S1. Animal- and probe-specific recording performance over time.

Number of	Electrodes (probes) implanted	functional electrodes	Electrodes Recorded spike	Electrodes w Stable spike	Single-unit	Stable SU
Mouse 1	12(4)	11	11	8	3	2
Mouse 2	8 (1)	6	2	2	1	1
Mouse 3	4 (1)	3	3	2	1	1
Mouse 4	16 (4)	11	9	7	3	3
Mouse 5	16 (2)	15	13	11	3	3
Mouse 6	24 (3)	22	22	22	4	4
Mouse 7	16 (2)	12	9	8	4	4
total	96 (16)	80	69	60	19	18

movie S1. A typical implantation procedure of the NET probe. Video showing a typical implantation procedure of the NET probe, recorded by a optical microscope from top view. The shuttle device (shown as the dark dot in the center) delivered a NET-50 probe into the brain. The reflection came from ACSF on the brain surface to float the NET probe and to reduce friction during insertion.

movie S2. The NET-vasculature integration 2 months after implantation. 3D reconstruction of *in vivo* 2P images showing integration of a NET-10 probe (red) and intact capillary network (green) two months post-implantation. Imaging depth: $100 - 320\ \mu m$ below the brain surface.

movie S3. In vivo 2P images of inactive astrocytes and intact capillary network around a folded segment of a NET-50 probe 3 months after implantation. The arrows mark the edge of the NET probe, where no astrocytic proliferation were observed. Imaging position and depth: $125 - 360\ \mu m$ below the brain surface.

movie S4. In vivo 2P images of neurons and two NET-10 probes 1.5 and 2.5 months after implantation. Intimate, non-degrading neuron-probe interface was observed. The capillaries were not fluorescently labeled and shown in dark. Imaging position and depth: $110 - 260\ \mu m$ below the brain surface.

movie S5. 3D reconstruction of in vivo 2P images of neurons and two NET-10 probes 1.5 months after implantation (the same images as in movie S4, left). Imaging depth: $110 - 260\ \mu m$.